applied optics

Multistatic fiber-based system for measuring the Mueller matrix bidirectional reflectance distribution function

Clifton G. Scarboro,[1,*] Colleen J. Doherty,[2] Peter J. Balint-Kurti,[3,4] and Michael W. Kudenov[1]

[1]Department of Electrical and Computer Engineering, North Carolina State University, 840 Oval Drive, Raleigh, North Carolina 27606, USA
[2]Department of Biochemistry, North Carolina State University, 120 W. Broughton Drive, Raleigh, North Carolina 27607, USA
[3]Plant Science Research Unit, USDA-ARS, Raleigh, North Carolina 27695, USA
[4]Department of Entomology and Plant Pathology, North Carolina State University, Raleigh, North Carolina 27695, USA
*Corresponding author: grant.scarboro@polarissensor.com

Received 15 July 2022; revised 6 October 2022; accepted 21 October 2022; posted 24 October 2022; published 14 November 2022

Bidirectionality effects can be a significant confounding factor when measuring hyperspectral reflectance data. The bidirectional reflectance distribution function (BRDF) can effectively characterize the reflectivity of surfaces to correct remote sensing measurements. However, measuring BRDFs can be time-consuming, especially when collecting Mueller matrix BRDF (mmBRDF) measurements of a surface via conventional goniometric techniques. In this paper, we present a system for collecting mmBRDF measurements using static optical fiber detectors that sample the hemisphere surrounding an object. The entrance to each fiber contains a polarization state analyzer configuration, allowing for the simultaneous acquisition of the Stokes vector intensity components at many altitudinal and azimuthal viewing positions. We describe the setup, calibration, and data processing used for this system and present its performance as applied to mmBRDF measurements of a ground glass diffuser.

https://doi.org/10.1364/AO.470608

1. INTRODUCTION

Light reflecting anisotropically from a surface creates complications when attempting to correlate optical measurements with a surface's physical properties [1–3]. Typically, light that reflects from an object can be estimated as a combination of specular (mirror-like) or Lambertian (diffuse) reflections [4], where specular reflections occur at the air–surface boundary, and Lambertian reflections result from, e.g., subsurface multiple scattering [5]. A light-scattering model that characterizes reflection as a function of the acquisition geometry, relative to an object's zenith, can enable the correction of remote sensing data for reflection effects caused by view-, surface normal-, and illumination-angle effects. The unpolarized bidirectional reflectance distribution function (BRDF) characterizes the anisotropic reflection of light that irradiates a surface as a function of the illumination, object, and viewing geometries, and it has been leveraged in applications spanning land topography [6], vegetation monitoring [7], and computer graphics rendering [8]. Beyond BRDF, the Mueller matrix BRDF (mmBRDF) provides even more optical information about a surface relating to material properties and micro-roughness than the unpolarized BRDF by further characterizing the polarized reflection response of the object [9]. The Mueller matrix generalizes the output polarization given any polarization state of light incident upon a surface.

Typically, BRDFs can be measured in a lab setting using a gonioreflectometer that consists of a light source and photodetector moving in various geometries around a sample [10]. The function of the gonioreflectometer can be extended to provide polarization measurements. For example, in [11], a three-axis goniometer provides measurements of a sample at any altitude and azimuth for a laser light source and detector, each with rotating retarder-fixed linear polarizer configurations for Mueller matrix acquisition. While this method provides excellent spatial resolution across the hemisphere, it is time-consuming, especially when using long detector exposure or signal averaging times. This can bring challenges when measuring surfaces that are rapidly changing [4], like a plant's leaf that has been detached and is actively senescing.

To decrease the data-acquisition time, multiple detectors may be used in an imaging gonioreflectometer to collect reflections from a sample at multiple viewing angles. For instance, Ward [12] used a hemispherical mirror surrounding a sample, which reflected light toward a CCD camera with a fisheye lens so that scanning is only done with the light source. While effective for unpolarized BRDF measurements, such a configuration is less

optimal for polarized BRDF measurements due to polarization effects from the mirror and the need for polarization optics with wide acceptance angles.

In this paper, we present a system for measuring the Mueller matrix BRDF using multimode optical fibers embedded at fixed locations in a hemisphere surrounding a target. Light output from the fibers is measured by multiple cameras simultaneously, and polarization sensitivity of each fiber is controlled using polarization optics affixed inside each fiber connector. In this way, the data-acquisition's speed is increased by eliminating the need for spatial and polarization scanning in the scattering directions. In Section 2, we describe the system principles of operation, setup, calibration, and testing methods. In Section 3, we provide the results of our simulations and real measurements of a ground-glass diffuser. In Section 4, we discuss the system performance, and we provide a conclusion in Section 5.

2. MATERIALS AND METHODS

A. mmBRDF Theory

In general, the BRDF is a function of the illumination and viewing geometry relative to the object's surface normal. As depicted in Fig. 1, the object with a surface normal (z axis) has an illumination incident vector, μ_i, with altitude, θ_i, and azimuth, ϕ_i. In addition, light scatter is observed along a viewing vector, μ_r, with altitude, θ_r, and azimuth, ϕ_r. For an azimuthal-invariant BRDF, only the azimuthal difference between the view and incident vectors is needed, such that $\Delta\phi = \phi_r - \phi_i$.

The light's polarization state is defined by the four elements of the Stokes vector ($\mathbf{S} = [\, S_0 \;\; S_1 \;\; S_2 \;\; S_3 \,]^{\mathrm{T}}$). Here, S_0 is the total radiance of light, S_1 is the excess of horizontally over vertically polarized light, S_2 is the excess of $+45°$ over $-45°$ polarized light, and S_3 is the excess of right-hand circular over left-hand circular polarized light [13–18]. The alteration of an input polarization state by an object is described by the 4×4 Mueller matrix, which relates an incident polarization state to a reflected or transmitted polarization state [19], such that

$$\mathbf{S_{out}} = \mathbf{M}\mathbf{S_{in}}. \tag{1}$$

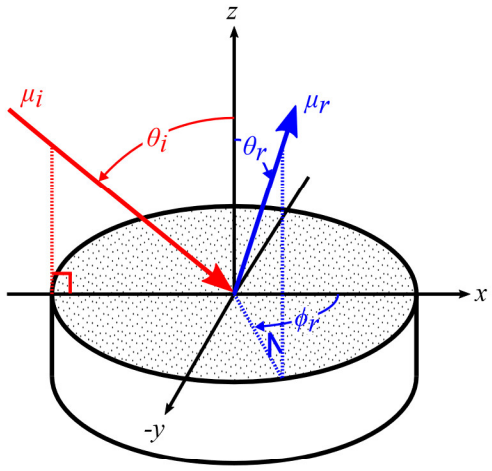

Fig. 1. Diagram of the BRDF angular conventions. The illumination vector, μ_i, and view vector, μ_r, are colored red and blue, respectively. The zenith angle corresponds to the z axis, and the illumination azimuth, ϕ_i, corresponds to the x axis.

The mmBRDF provides Mueller matrices describing diffuse and specular reflections across a range of incidence and scattering angles [20].

To measure a full Mueller matrix, a polarimeter with a complete polarization state analyzer (PSA) and polarization state generator (PSG) is required [21]. One of the most common ways to construct a Mueller matrix polarimeter is with a dual-rotating quarter-wave plate (QWP) system, with fixed linear polarizers, to obtain many different PSA and PSG settings [22,23]. Alternatively, another type of Mueller matrix polarimeter uses a four-detector polarimeter with four (or more) PSA settings and the conventional rotating QWP-fixed polarizer PSG [24,25].

In general, for arbitrary PSA and PSG settings, the detector's intensities can be calculated by

$$\begin{pmatrix} I_{11} & \cdots & I_{1N} \\ \vdots & \ddots & \vdots \\ I_{M1} & \cdots & I_{MN} \end{pmatrix} = \begin{pmatrix} \mathbf{A}_1 \\ \mathbf{A}_2 \\ \vdots \\ \mathbf{A}_M \end{pmatrix} \begin{pmatrix} m_{11} & m_{12} & m_{13} & m_{14} \\ m_{21} & m_{22} & m_{23} & m_{24} \\ m_{31} & m_{32} & m_{33} & m_{34} \\ m_{41} & m_{42} & m_{43} & m_{44} \end{pmatrix} \begin{pmatrix} \mathbf{G}_1 & \mathbf{G}_2 & \cdots & \mathbf{G}_N \end{pmatrix}, \tag{2}$$

where $\mathbf{I}$ contains the measured intensities, $\mathbf{A}_m$ is the analyzer vector (S_0 sensitivity to each incident Stokes parameter) describing the m^{th} PSA configuration, $\mathbf{M}$ is the sample's Mueller matrix, and $\mathbf{G}_n$ is the generator vector (output Stokes vector given incident unpolarized light) describing the n^{th} PSG configuration.

B. mmBRDF Modeling

There are models that can predict a surface's mmBRDF based on the surface's light-scattering and physical properties [26–28]. With our reflectance measurements, we attempt to fit a model that includes both diffuse and specular reflection components. The model treats light as a bulk of scattering particles instead of a wavefront with diffraction and interference properties. Furthermore, we use a model that has no circular polarizing component, which is typical of plant targets [29]. In this way, we use prior information about the mmBRDF's shape via a mathematical model to supplement our measurements and produce a more accurate characterization. The overall form of the model is given by

$$\mathbf{f}(\theta_r, \theta_i, \Delta\phi) = a\mathbf{f}_{\mathbf{diff}}(\theta_r, \theta_i) + b\mathbf{f}_{\mathbf{facet}}(\theta_r, \theta_i, \Delta\phi), \tag{3}$$

where $\mathbf{f}_{\mathbf{diff}}$ and $\mathbf{f}_{\mathbf{facet}}$ are volumetric (diffuse) and microfacet (specular) contributions to the model and are superposed and scaled by the factors a and b, respectively. The expression for $\mathbf{f}_{\mathbf{diff}}$ is a diffuse subsurface model presented by Germer [26] and is given as

$$\mathbf{f}_{\mathbf{diff}}(\theta_r, \theta_i) = \mathbf{M}_{\mathbf{diff}} \frac{(\rho/\pi)}{(1 - \rho\bar{R})} \frac{\cos\theta_r' \cos\theta_i'}{\cos\theta_r \cos\theta_i}, \tag{4}$$

where the reflectance is ρ; the incident and scattering directions into the surface are θ_i' and θ_r', respectively, and are determined by Snell's law; $\bar{R}$ is the calculated reflectance of the top of the surface based on the internal reflection coefficients; and $\mathbf{f}_{\mathbf{facet}}$ is

a shadowed facet scattering model derived by Barrick [27] for Mueller matrices as

$$\mathbf{f}_{\mathbf{facet}}(\theta_r, \theta_i, \Delta\phi) = \pi \sec^4\gamma\, p(\zeta_{xsp}, \zeta_{ysp})\mathbf{R}_{\mathbf{mm}}(\iota)\sqrt{S(\theta_i)S(\theta_r)}, \tag{5}$$

where γ is the angle between the surface normal (mean microfacet normal) and the microfacet normal at the specular point, $p(\zeta_{xsp}, \zeta_{ysp})$ is the probability distribution function (PDF) of the microfacets' slopes, and ζ_{xsp} and ζ_{ysp} are slopes in the x and y directions, respectively. In our calculations, we use an exponential PDF, defined as

$$p(\zeta_{xsp}, \zeta_{ysp}) = \frac{3}{\pi s^2}\exp\left(-\sqrt{6(\zeta_{xsp}^2 + \zeta_{ysp}^2)/s^2}\right), \tag{6}$$

where s is the root-mean-square of the surface slope. Instead of s, in this paper, we use the parameter, σ, which is the standard deviation of the polar angle of the microfacets' surface normal. Furthermore, for $\mathbf{R}_{\mathbf{mm}}(\iota)$ in Eq. (5), we used the reflection coefficients as derived by Mitzner [30] and converted for Mueller matrices using the Bohren and Huffman algorithm [31] for a local angle of incidence at the microfacet ι. The reflection coefficients have a dependency on the material's index of refraction, n, and attenuation coefficient, k. Finally, $S(\theta)$ is a shadowing function, which in this paper is the Smith shadow function [32] with a standard deviation parameter, w. In total, there are seven parameters that can be used to fit the model in Eq. (3): a, b, n, k, ρ, σ, and w. This model was implemented using the SCATMECH library [28] of scattering codes.

C. System Description and Construction

The system we have built for mmBRDF measurements consisted of illumination and detector components pointing toward a central point where a target specimen is placed. A concept diagram and photo of the constructed system are shown in Fig. 2. A 2000 mW broadband light-emitting diode (LED) (Thorlabs MWWHLP1) illuminator was mounted on an arm that rotates in altitude (θ_i) using a rotation stage (Thorlabs HDR50). A six-position motorized filter wheel (Thorlabs FW102C) was mounted in front of the LED, which contained 10 nm full-width half maximum (FWHM) bandpass spectral filters. In this paper, the only utilized filter has a center-pass band located at 550 nm, while the other filters are reserved for future use. The PSG was also mounted on the LED arm. The PSG contained a linear polarizer, with its transmission axis set to 0° (transverse electric [TE] polarization relative to the plane of incidence) and an achromatic QWP mounted on a piezoelectric rotation stage (Thorlabs ELL14). Light output from the PSG illuminated the sample, which was placed on an adjustable-height platform.

1. Fiber Hemisphere and Alignment

Centered over the top of the sample is a steel hemisphere with a diameter of 305 mm. Holes were drilled in locations along the LED azimuthal location so that light could enter the hemisphere at multiple altitudes. The sphere's interior was painted a matte black color so as to minimize internal reflections within the system. Multimode fibers were mounted to FC connectors, which were epoxied into drilled holes in the hemisphere. We used multimode fibers instead of monomode or polarization-maintaining (PM) fibers in order to achieve higher radiometric throughput. The connectors have random locations, which were determined by simulation in MATLAB (see Table S1 in Supplement 1) but were biased in the forward-scattering direction. The reasoning for this is that there are typically more rapid variations in intensity versus angle in the forward-scattering direction, and more detectors yielded more accurately fitted and interpolated results in our simulations. In addition, the positions were constrained such that no fiber was superposed with another fiber or calibration hole. On each fiber connector is one of four different PSA optics: a linear polarizer at 0° (LP0); a linear polarizer at 45° (LP45); a linear polarizer at 90° (LP90); or a QWP at 45° bonded to a linear polarizer at 0°, forming a right-hand circular (RHC) analyzer. In total, there were 280 fibers evenly distributed between each of the four PSAs.

A critical aspect during assembly was to align the fiber connectors' polarization optics properly to the sample's place of incidence. The procedure for aligning the connectors on the hemisphere is depicted in Fig. 3. In addition to the holes drilled for each connector, 280 smaller corresponding calibration holes were drilled, which were at the same altitude as each connector hole but rotated 180° in azimuth. During the alignment of a connector containing a linear polarizer, the hemisphere was oriented such that light from an LED passed through a calibration hole and reflected from a polished silicon wafer, placed in the center of the hemisphere. Reflected light was directed toward the connector that was being rotationally aligned to the plane of incidence. Specular reflections from polished silicon

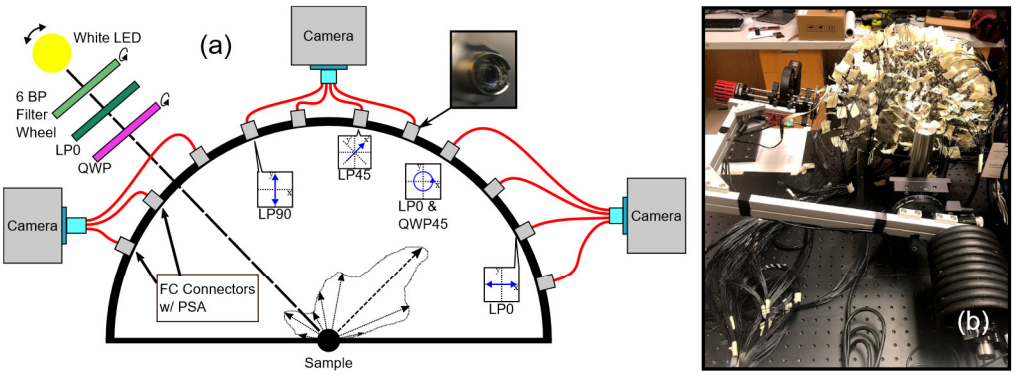

Fig. 2. (a) Diagram of fiber-based mmBRDF system. (b) Photograph of constructed fiber-based mmBRDF system.

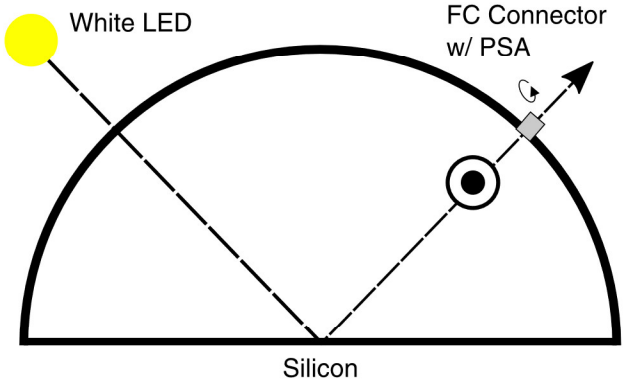

Fig. 3. Depiction of the alignment of polarization connectors in mmBRDF system. Light enters the hemisphere through a calibration hole and reflects from the silicon, becoming TE polarized. The connector with PSA elements is placed in its hole so that it receives specularly reflected light. As the connector is rotated, the measured intensity behind it changes.

are TE polarized [33], so an LP can be aligned by rotating the connector in its location and measuring the light output with a camera behind the connector. When a maximum intensity is measured, the LP is oriented with its transmission axis perpendicular to the plane of incidence (0°). Conversely, a minimum intensity is measured when the LP is oriented with its transmission axis inside the plane of incidence (90°). When the intensity is halfway between the maximum and minimum, the LP is either oriented to 45° or 135°, so the transmission axis was roughly marked on the connector prior to alignment to remove this ambiguity. A fast-curing two-part epoxy was then used to fix the connector into its hole. Generally, we estimate that the transmission axis alignment error is on the order of ±2.5% based on the contrast in intensity between the 0° and 90° orientations of a connector. For the RHC connectors, the QWP and LP were bonded together with a UV-cured optical adhesive before being cut and bonded into the fiber connector. The RHC connectors were then aligned in the same way as the LP connectors by leveraging the spectral dependence of the QWPs. The QWPs have an optical path difference (OPD) of 140 nm (i.e., a quarter wave at a wavelength of 560 nm), so by using a red LED (660 nm wavelength) as the light source, optimal alignment to the plane of incidence was achieved when the RHC connectors transmitted a maximum intensity. It should be noted that, if the QWP material were achromatic, rotating the RHC in the mount would have provided little to no variation in the transmitted light intensity, yielding a more challenging optical alignment of the connector to the plane of incidence.

2. Fiber Array and Camera Control

Twenty-four fibers make up a single fiber array (Precision Micro-Optics, F2281852), and two fiber arrays were coupled to each Raspberry Pi HQ Camera with the infrared filter removed. To minimize cross-talk between adjacent fiber channels, the fibers needed to be placed closer to the detector's pixels than the coverglass initially allowed (the coverglass is approximately 1 mm thick). The coverglass of each camera was sanded down to an overall thickness of approximately 0.5 mm using 250 grit sandpaper. Any optical scattering that arose due to the rough surface was resolved from the index of refraction matching when the fiber face was subsequently glued to the coverglass. Additional information on the system's construction can be found in Supplement 1. A total of six cameras were interfaced by "secondary" Raspberry Pi 4B computers. A seventh "primary" Raspberry Pi 4B controlled the data-acquisition process by triggering the secondary computers to collect images and send them to the primary computer. The primary computer also controls the LED arm, filter wheel, and QWP rotation stage. During a typical data acquisition, several configurations of the motors are swept through, and, at each state, images from the cameras are captured at multiple exposure times to accommodate the large dynamic range of the BRDF. The data are then transferred to a lab computer for image processing.

Each acquired image has up to 48 channels arranged in a 2×24 array pattern of spots corresponding to outputs from specific fibers. Example raw images are shown in Supplement 1 in Fig. S3. The raw images were converted to monochrome images by averaging the red, green, and blue pixels in each Bayer array 2×2 "super" pixel. A dark frame, where an image was taken with the LED blocked by blackout fabric, was subtracted from the data taken at the same exposure time. Then, a 5×5 pixel window was sampled from the center of each fiber spot and averaged to yield the intensity for that fiber. Each fiber from the images was then correlated with its physical location (altitude and azimuth) on the hemisphere to facilitate further processing. All images were then scaled by a ratio of their exposure times to the shortest exposure time used during data acquisition, such that all fiber measurements were on the same intensity scale. Finally, the data were normalized to measurements taken of the spectralon to account for systemic alignment disparities, blur, and other issues associated with our optical elements. Because the spectralon is not perfectly Lambertian, the measurements were further normalized to readily available models of the mmBRDF of spectralon [34]. The normalized measurement, I_{norm}, is given as

$$I_{\text{norm}}(\theta_r, \theta_i, \Delta\phi) = \frac{I_{\text{sample}}(\theta_r, \theta_i, \Delta\phi)}{I_{\text{tile}}(\theta_r, \theta_i, \Delta\phi, \lambda)/I_{\text{model}}(\theta_r, \theta_i, \Delta\phi)}, \tag{7}$$

where I_{sample} are the target intensities, I_{tile} are the intensity measurements of the spectralon reference tile, and I_{model} are the model's intensities of a theoretical spectralon measurement. Wavelength dependence is also implied for this calculation.

D. Simulations and Data Processing

Prior to building the system, simulations were conducted in MATLAB to characterize its potential performance in quantifying the mmBRDF of samples. A target mmBRDF was generated in MATLAB by applying Eq. (3) with parameters selected so that they were approximate to what would be expected in natural targets like a plant leaf [35]. For θ_i ranging from 0° to 45° in 15° increments, and the generator QWP angle, θ_G, ranging from 22.5° to 157.5° in 22.5° increments, we sampled the model at each viewing vector, μ_r, corresponding to the fibers' locations on the hemisphere. Based on the PSA, we calculated the measured intensity for each fiber using the relationship

in Eq. (2) with a single fiber's analysis vector and obtained a measured intensity for each PSG configuration and incident vector, μ_i. Poisson noise was then applied to the simulated measurement to give a signal-to-noise ratio (SNR) of 100. We simulated the reconstruction procedure from the array of sparsely sampled intensities to identify potential sources of error. Because of the setup, we do not have measurements from all four PSA configurations at any one μ_r. Consequently, we had two methods to reconstruct the results, which we use for our simulated measurements and experimental data. The first method interpolates the I_0, I_{45}, I_{90}, and I_{RHC} measurements across the entire hemisphere using Delaunay triangulation and then uses the relation in Eq. (2) to solve for the Mueller matrix of the sample at any query vector μ_r. The second method fits the measured data to the seven-parameter model by minimizing the root-mean-square deviation (RMSD) between the measured and model intensities. This involved a coarse-search across a wide range of realistic model parameters, followed by a fine fitting of the parameters using the Nelder–Meade simplex method [36]. In our system analysis, we have omitted fibers with $\theta_r > 70°$ due to the decreased margin of error in the height alignment for these altitudes, where some fibers could potentially be viewing the side of a target instead of the top surface. As a result, only the measurements of 218 out of 280 fibers are presented in this paper.

1. Experimental Validation

For validation of our system, we took measurements of a 600 grit ground-glass diffuser (GGD, Thorlabs DG20-600). We painted the smooth side of the GGD with black matte paint and collected measurements with the diffuse side facing upward. This simplified the BRDF model by reducing reflections from the underside of the GGD and also provided measurements of a target with a known surface roughness. We also collected polarization BRDF measurements of the GGD along the plane of incidence using a helium–neon (HeNe) laser and Sony Lucid Vision polarization camera (Phoenix IMX250MZR/MYR) by moving the camera to various altitudes in relation to the GGD. The incident light was TE polarized using a linear polarizer so that we could make comparisons with the BRDF measurements in our constructed system. We used the HeNe laser because of its intensity stability over time when compared with other lasers or laser diodes readily available. It should be noted that the HeNe laser emits light at 632.8 nm, while our fiber-based BRDF data are collected with 550 nm light. Since the refractive index, n, of the BK7 glass is the primary spectral dependence, we only expect this difference to cause a deviation of $\approx 1.1\%$ between the BRDF measurements of the ground glass diffuser, based on the Fresnel reflectances at each band at normal incidence.

3. RESULTS

A. Simulations

Simulations were performed to quantify the errors of the interpolation and model fitting reconstruction methods. We provide a sample of the results from the simulation analysis in Figs. 4 and 5 for azimuthal planes of 30° and 60°, respectively. The target model Stokes parameters given incident unpolarized light are plotted alongside the linearly interpolated and model fitting reconstructions. The parameters for the target model were $a = 1$, $b = 1$, $n = 1.5$, $k = -0.01$, $\rho = 0.1$, $\sigma = 25$, and $w = 0.1$. The parameters determined by the model fitting were $a = 1.2024$, $b = 0.7657$, $n = 1.4955$, $k = -0.0252$, $\sigma = 27.7551$, $\rho = 0.1270$, and $w = 0.0501$. The errors are

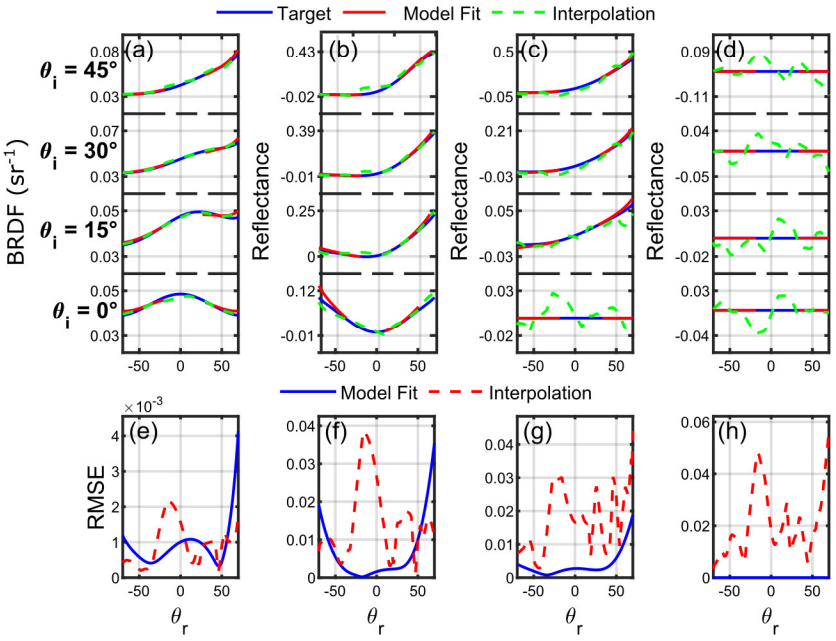

Fig. 4. Simulation of linear interpolation and model fitting to simulated target BRDF with plots along 30° azimuthal plane. The reconstructions and target BRDF are shown by Stokes vector as (a) S_0, (b) S_1/S_0, (c) S_2/S_0, and (d) S_3/S_0, and the RMSE for each reconstruction method is shown for each Stokes parameter in (e) S_0, (f) S_1/S_0, (g) S_2/S_0, and (h) S_3/S_0.

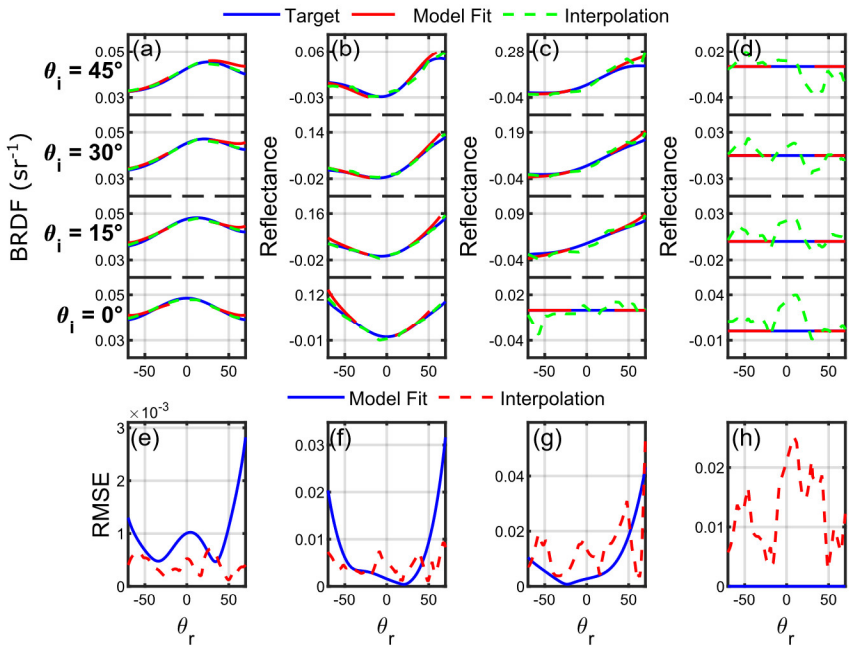

Fig. 5. Simulation of linear interpolation and model fitting to simulated target BRDF with plots along 60° azimuthal plane. The reconstructions and target BRDF are shown by Stokes vector as (a) S_0, (b) S_1/S_0, (c) S_2/S_0, and (d) S_3/S_0, and the RMSE for each reconstruction method is shown for each Stokes parameter in (e) S_0, (f) S_1/S_0, (g) S_2/S_0, and (h) S_3/S_0.

smaller overall when using the model fitting when compared with that of the linear interpolation reconstruction.

The average linear interpolation root-mean-square error (RMSE) for each Stokes parameter was [0.0104 0.0552 0.0705 0.0276], while the average model RMSE was [2.718×10^{-3} 0.0162 0.0095 8.4847×10^{-19}]. It is also worth mentioning that the S_3 component always holds a value of 0 for the model we are using, which leads to greater noise impact on the linear interpolation method for S_3. In general, it seems that, when a Mueller matrix element is close to 0 in actuality, the RMSE increases for an interpolation. A more comprehensive compilation of the simulation results is presented in Supplement 1.

B. Ground Glass Diffuser Measurements

Results from the measurement of a 600 grit GGD with 550 nm light have been compiled here. The acquisition time for this single band with exposure times at 100, 250, 500, and 1000 ms, four θ_i angles, and seven θ_G angles, was approximately 46 min. It should be mentioned that this measurement time is primarily limited by software, with primary bottlenecks being the use of the "raspistill" command, which was called by each of the six secondary computers from the primary computer. Using an alternative to raspistill (e.g., OpenCV), which initializes and closes the camera upon each call, would reduce the time by an estimated factor of 5, bringing potential total measurement time down to 9 min. The model fitting of the data resulted in parameters of $a = 1.3735$, $b = 0.7346$, $n = 1.5648$, $k = -0.0216$, $\rho = 0.0210, \sigma = 42.3773$, and $w = 0.1013$.

Given that the BK7 glass that makes up the GGD has an index of refraction of approximately 1.52 and attenuation coefficient close to 0 [37], it is encouraging that the model fitted these parameters closely with an error of 3.05% in n. In Fig. 6, we plotted the intensity data and corresponding model fitting after tile normalization according to fiber index for $\theta_i = 0°$, 15°, 30°, and 45°. This allows for a comparison of our measurements and the model across all fibers. The RMSD between the data and model for each fiber are also shown in Fig. 6. The average deviations by fiber PSA type, in units of sr^{-1}, are $I_{0,\mathrm{RMSD}} = 1.301 \times 10^{-3}$, $I_{45,\mathrm{RMSD}} = 9.5014 \times 10^{-4}$, $I_{90,\mathrm{RMSD}} = 8.7277 \times 10^{-4}$, and $I_{\mathrm{RHC,RMSD}} = 9.0493 \times 10^{-4}$. The average overall deviation across all fibers is 1.0072×10^{-3}.

To provide a better sense of the fiber locations in the BRDF and their respective measurements, we have included Fig. 7, which plots the data and model for the fibers located along a range of azimuthal planes spanning 20°. It should be mentioned that many of the plots take on a "jagged" or discontinuous appearance, which is caused by the measurements' inability to sample points from a single azimuth because of their sparse and randomly selected measurement locations. Despite this, we can observe that I_0 takes on larger values in the specular direction ($\Delta\phi = 0°$), while I_{90} is largest when the azimuth is orthogonal to this plane ($\Delta\phi = 90°$). Also, the intensity is brighter along the specular direction when θ_i is higher, while it remains mostly constant on the orthogonal plane.

In Fig. 8, we present our system BRDF measurements and model fitting within the incident plane alongside BRDF measurements taken with the HeNe laser for an incident altitude of 30°. These results are given to help validate the accuracy of our system. We can see from these plots that the polarized BRDF data from our system aligns fairly closely to the HeNe measurements. The shape of the plots do not follow as closely in I_{90}, which is to be expected since the measurement intensity is smaller compared with I_0. The RMSEs between the system measurements and the HeNe measurements by

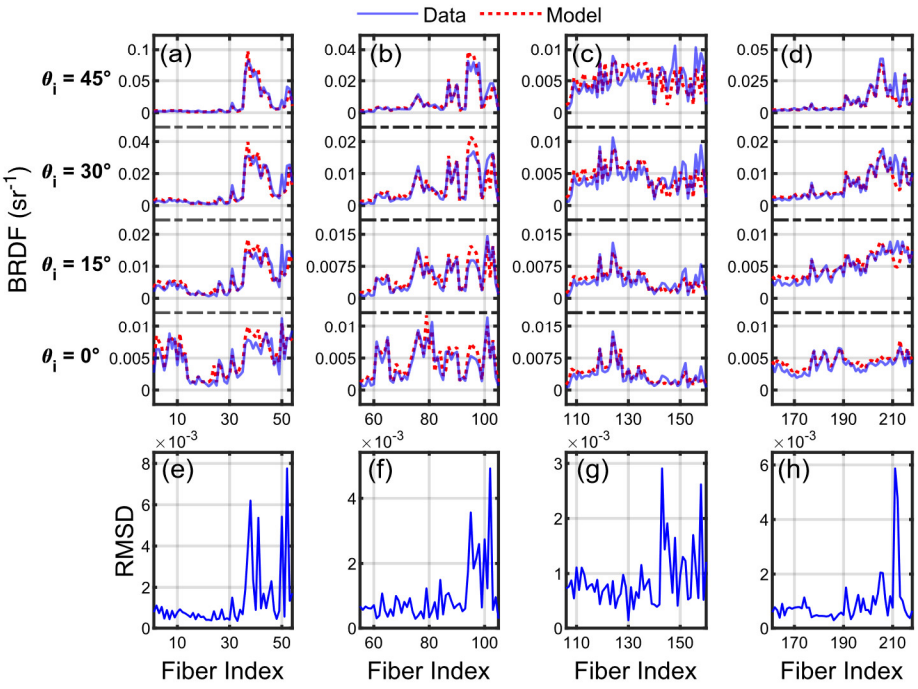

Fig. 6. Plots of 550 nm spectralon-normalized measurements of the ground glass diffuser alongside the model fit by fiber index for (a) I_0 fibers, (b) I_{45} fibers, (c) I_{90} fibers, and (d) I_{RHC} fibers. We also plot the RMSD between the model and data by fiber index for (e) I_0 fibers, (f) I_{45} fibers, (g) I_{90} fibers, and (h) I_{RHC} fibers.

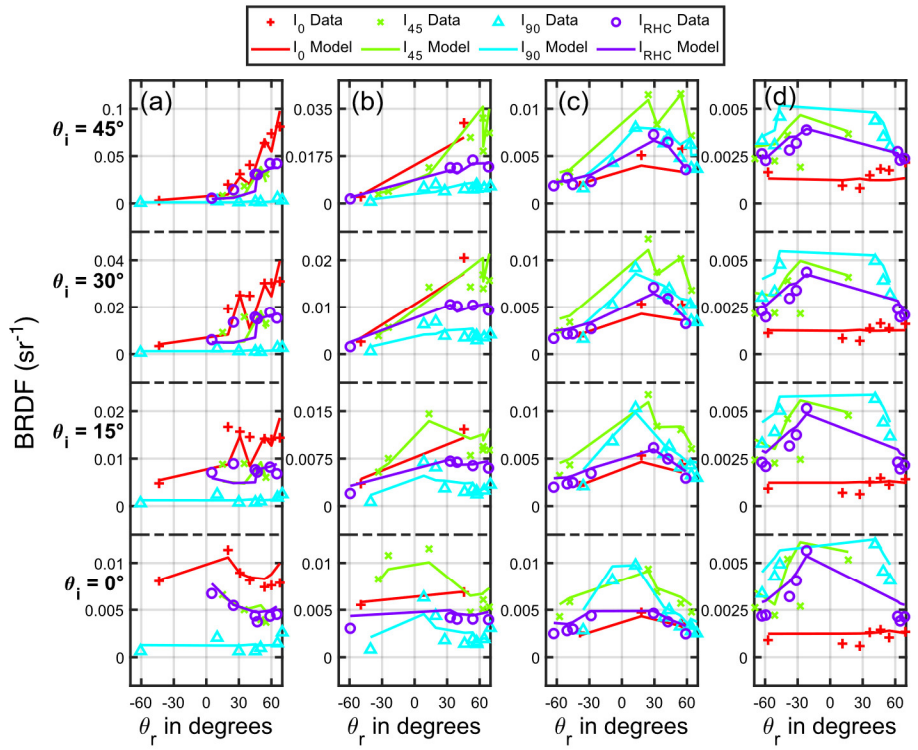

Fig. 7. Plots of fiber measurements and model fit with light incident at 0°, 15°, 30°, and 45° in altitude, $\theta_G = 90°$, and viewing vectors along an azimuthal range of (a) $0° \pm 10°$, (b) $30° \pm 10°$, (c) $60° \pm 10°$, and (d) $90° \pm 10°$.

fiber PSA type are 2.7653×10^{-3} for I_0, 3.0665×10^{-3} for I_{45}, and 1.2258×10^{-3} for I_{90}, and the overall RMSE is 2.4868×10^{-3}. The RMSEs between the model fit and the HeNe measurements by fiber PSA type are 4.0855×10^{-3} for I_0, 2.2247×10^{-3} for I_{45}, and 6.4191×10^{-4} for I_{90}, and the overall RMSE is 2.7174×10^{-3}.

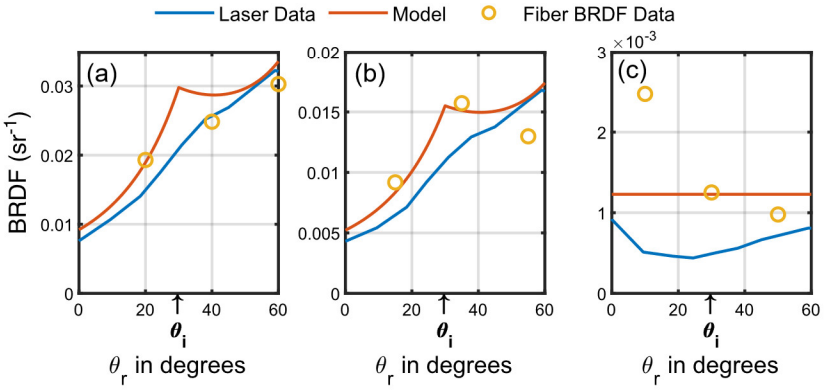

Fig. 8. HeNe laser BRDF data (632.8 nm), model fit, and fiber-based mmBRDF system data (550 nm) plotted for $\theta_i = 30°$ with measurements in (a) I_0, (b) I_{45}, and (c) I_{90}.

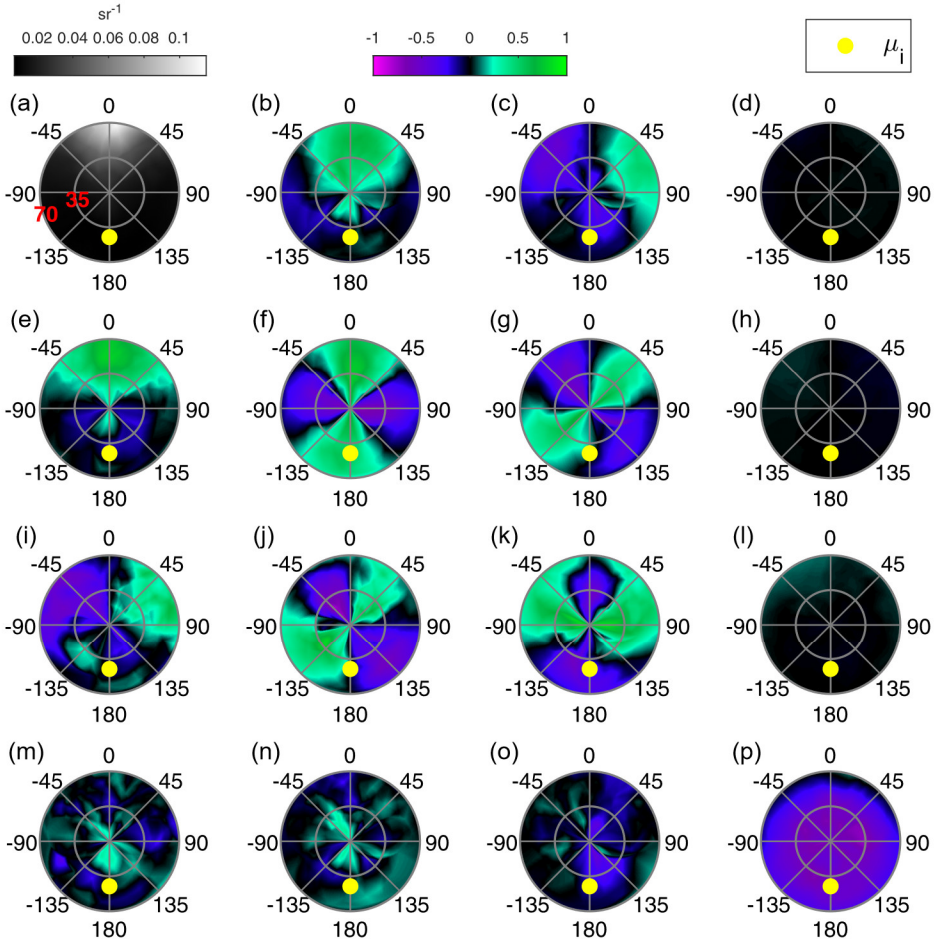

Fig. 9. Linear interpolation Mueller matrix color-mapped plots of 600 grit ground-glass diffuser at 550 nm and $\theta_i = 45°$. The plane of incidence corresponds to an azimuth of 0°. The data were linearly interpolated to evaluate reflectances across the hemisphere, and the corresponding Mueller matrix was calculated. The viewing altitude (radial) axis labels are shown in red text in (a) as linearly increasing angles and are the same increments for each plot. The azimuthal (angular) axis labels are shown on all plots in black. The Mueller elements are (a) m_{11}, (b) m_{12}, (c) m_{13}, (d) m_{14}, (e) m_{21}, (f) m_{22}, (g) m_{23}, (h) m_{24}, (i) m_{31}, (j) m_{32}, (k) m_{33}, (l) m_{34}, (m) m_{41}, (n) m_{42}, (o) m_{43}, and (p) m_{44}.

For $\theta_i = 45°$, Fig. 9 shows color-mapped polar plots of the Mueller matrix measured by the system using the linear interpolation method of the reconstruction. Likewise, Fig. 10 shows the fitted models as color-mapped polar plots. In Supplement 1, we provide similar color-mapped plots for the model fitting and interpolated results at 0°, 15°, and 30° incidence altitudes. Here, we can see the shape of the mmBRDF in two dimensions and perform an overall comparison between the linear interpolation and model fitting reconstructions. The interpolated plots have a general shape consistent with expectations for a GGD,

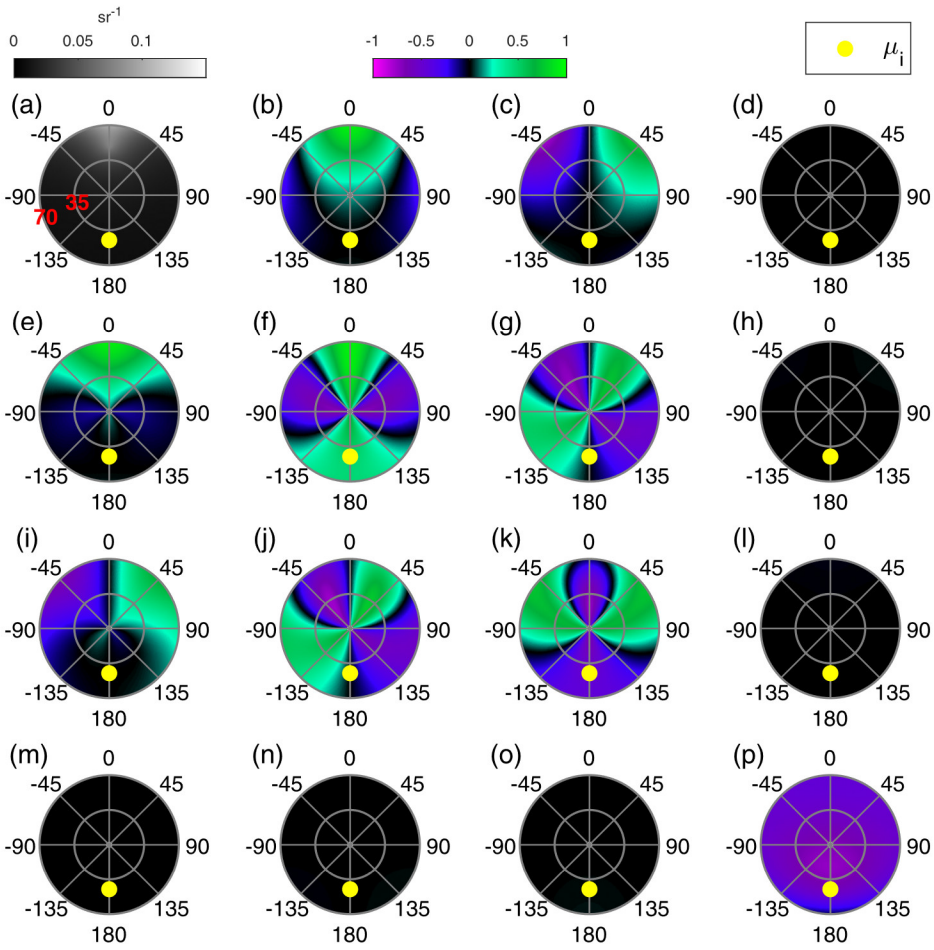

Fig. 10. Model fit Mueller matrix color-mapped plots of 600 grit ground-glass diffuser at 550 nm and $\theta_i = 45°$. The plane of incidence corresponds to an azimuth of 0°. The data were used to fit the parameters of a combined diffuse and microfacet scattering model. The viewing altitude (radial) axis labels are shown in red text in (a) as linearly increasing angles and are the same increments for each plot. The azimuthal (angular) axis labels are shown on all plots in black. The Mueller elements are (a) m_{11}, (b) m_{12}, (c) m_{13}, (d) m_{14}, (e) m_{21}, (f) m_{22}, (g) m_{23}, (h) m_{24}, (i) m_{31}, (j) m_{32}, (k) m_{33}, (l) m_{34}, (m) m_{41}, (n) m_{42}, (o) m_{43}, and (p) m_{44}.

but there are certain elements, particularly those related to circular polarization, where the plots appear noisy or asymmetrical. The model fitting corrects for this because it is primarily a linear polarization model, and the other elements also have a much smoother shape overall. We have provided color-mapped polar plots of the RMSD between the fitted model and interpolated data in Fig. 11, averaged over all θ_i values we have collected data for. We observe that the largest differences between the model and interpolated measurements occur at areas of the mmBRDF where the function changes quickly versus the viewing angle. The RMSD between the fitted model and data interpolation averaged across all Mueller elements is 0.1351.

4. DISCUSSION

Our simulations demonstrated some of the drawbacks of our system design when trying to achieve a more conventional measurement approach in which model fitting is not well-integrated or intended. Because we do not sample each PSA at a single viewing location, there are inherent errors in the reconstruction when trying to interpolate the results and obtain the mmBRDF for all viewing geometries. These errors would not be present in goniometric mmBRDF acquisition techniques. For instance, we see many of the interpolation errors reflected in the simulations that also become apparent in our measurements of the GGD. Values determined for m_{41} by the linear interpolation reconstruction are noisy because this element is nearly 0 for a GGD, and the measurements seen are largely artifacts of the reconstruction.

Beyond interpolation, we have also demonstrated that the sparse measurements can be supplemented with known information about how the surface should scatter light based on its structure. This comes in the form of a BRDF model that gives the expected shape of the measurements and has fittable parameters. Overall, this provides a more consistent fit that generally follows the trends of the linear interpolation but suffers less from artifacts and error caused by the interpolation. The linear interpolation and model-fitting techniques appear to have the same general shape, with error on the order of 10%, and align with BRDF measurements taken with the HeNe laser (error on order of 0.1%).

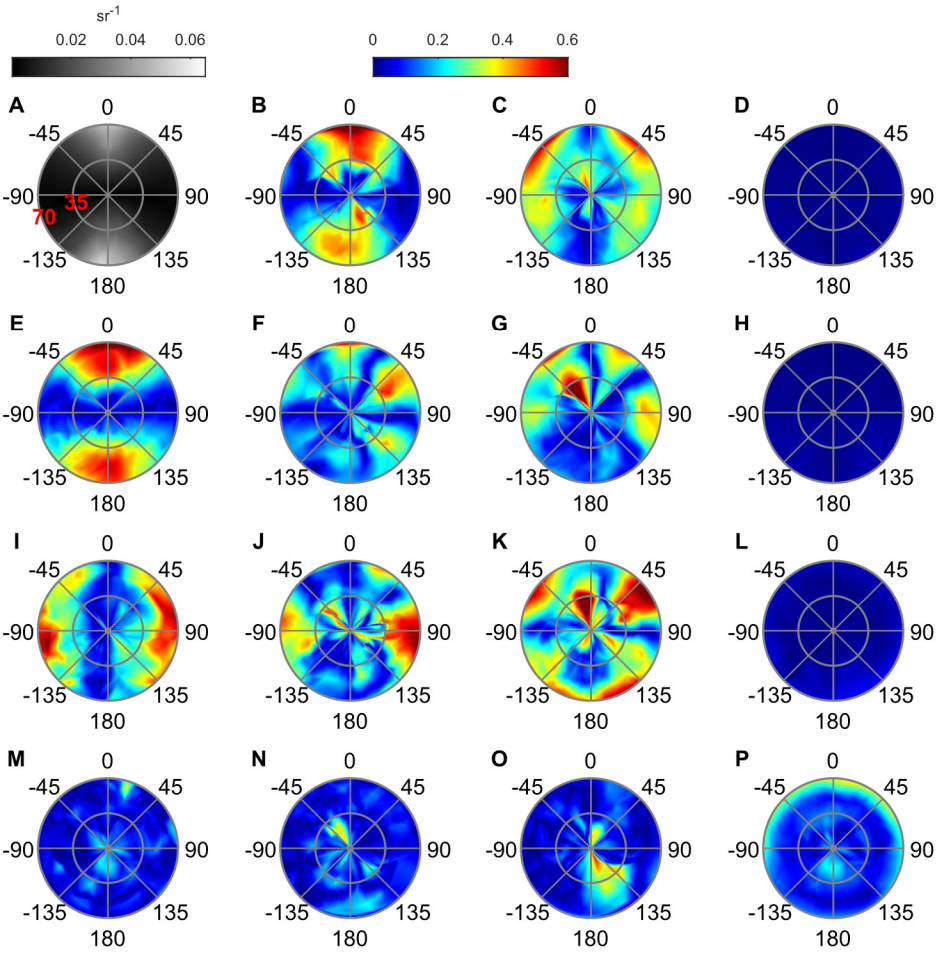

Fig. 11. RMSD between model fit and linear interpolation reconstructions of the Mueller matrix. The viewing altitude (radial) axis labels are shown in red text in (a) as linearly increasing angles and are the same increments for each plot. The azimuthal (angular) axis labels are shown on all plots in black. The Mueller elements are (a) m_{11}, (b) m_{12}, (c) m_{13}, (d) m_{14}, (e) m_{21}, (f) m_{22}, (g) m_{23}, (h) m_{24}, (i) m_{31}, (j) m_{32}, (k) m_{33}, (l) m_{34}, (m) m_{41}, (n) m_{42}, (o) m_{43}, and (p) m_{44}.

The advantage our system has over the goniometric acquisition method is largely the speed of data acquisition. The lack of scanning in the viewing angle of our system eliminates a time-consuming process at a cost of having a fixed spatial resolution. A goniometric mmBRDF system with 36 rotating-retarder configurations, 50 viewing angles, and one exposure time at each position would require 450 more acquisition periods than our system, in addition to the time needed to move the detector via rotation stages. This time-efficient design would be particularly useful in characterizing biological targets in a controlled laboratory setting, where a leaf is clipped from a plant, and it is necessary to collect measurements quickly before leaf senescence. Our system could be further optimized for shorter measurement times by reducing the overhead brought by the creation/destruction of the camera capture process through the use of the OpenCV library. In addition, the use of a brighter light source would shorten exposure times required for high SNR measurements in the system.

5. CONCLUSION

This paper described a novel method of acquiring mmBRDF measurements of samples in a quick manner. We performed simulations of the system to determine its feasibility prior to its construction and found the model fitting to be more accurate for processing the measurements. We then built the system using many detectors on a steel hemisphere centered on a sample and fiber arrays that couple the light to six Raspberry Pi cameras that measure the viewing light intensity without spatial sweeping or PSA configuration scanning. We processed the measurements of a ground-glass diffuser by linearly interpolating the polarization measurements and by fitting them to a microfacet/diffusion BRDF model. We found our system's measurements to be accurate, but on the order of 100× faster in acquisition than typical goniometric BRDF devices.

Funding. National Institute of Food and Agriculture (2020-67021-31961); Division of Electrical, Communications and Cyber Systems (1809753).

Disclosures. The authors declare no conflicts of interest.

Data availability. Data underlying the results presented in this paper are not publicly available at this time but may be obtained from the authors upon reasonable request.

Supplemental document. See Supplement 1 for supporting content.

REFERENCES

1. S. Vanonckelen, S. Lhermitte, and A. Van Rompaey, "The effect of atmospheric and topographic correction methods on land cover classification accuracy," Int. J. Appl. Earth Obs. Geoinf. **24**, 9–21 (2013).
2. V. Balthazar, V. Vanacker, and E. F. Lambin, "Evaluation and parameterization of ATCOR3 topographic correction method for forest cover mapping in mountain areas," Int. J. Appl. Earth Obs. Geoinf. **18**, 436–450 (2012).
3. S. Lhermitte, J. Verbesselt, W. W. Verstraeten, and P. Coppin, "A comparison of time series similarity measures for classification and change detection of ecosystem dynamics," Remote Sens. Environ. **115**, 3129–3152 (2011).
4. A. W. Bailey, E. A. Early, K. S. Keppler, V. I. Villavicencio, P. Kennedy, R. J. Thomas, J. J. Zohner, and G. Megaloudis, "Dynamic bidirectional reflectance distribution functions: measurement and representation," J. Laser Appl. **20**, 22–36 (2008).
5. L. B. Wolff, "Relative brightness of specular and diffuse reflection," Opt. Eng. **33**, 285–293 (1994).
6. P. Nina, W. Kun, L. Tao, and P. Yang, "Research of BRDF effects on remote sensing imagery," Proc. SPIE **8194**, 144–150 (2011).
7. G. Roberts, "A review of the application of BRDF models to infer land cover parameters at regional and global scales," Prog. Phys. Geogr. **25**, 483–511 (2001).
8. J. T. Kajiya, "The rendering equation," ACM SIGGRAPH Comput. Graph. **20**, 143–150 (1986).
9. J. L. Pezzaniti, R. A. Chipman, and S. C. McClain, "Polarization BRDF," Proc. SPIE **2260**, 160–167 (1994).
10. C. Schwartz, R. Sarlette, M. Weinmann, M. Rump, and R. Klein, "Design and implementation of practical bidirectional texture function measurement devices focusing on the developments at the University of Bonn," Sensors **14**, 7753–7819 (2014).
11. T. A. Germer and C. C. Asmail, "Goniometric optical scatter instrument for out-of-plane ellipsometry measurements," Rev. Sci. Instrum. **70**, 3688–3695 (1999).
12. G. J. Ward, "Measuring and modeling anisotropic reflection," ACM SIGGRAPH Comput. Graph. **26**, 265–272 (1992).
13. D. J. Diner, A. Davis, B. Hancock, G. Gutt, R. A. Chipman, and B. Cairns, "Dual-photoelastic-modulator-based polarimetric imaging concept for aerosol remote sensing," Appl. Opt. **46**, 8428–8445 (2007).
14. D. J. Diner, A. Davis, B. Hancock, S. Geier, B. Rheingans, V. Jovanovic, M. Bull, D. M. Rider, R. A. Chipman, A.-B. Mahler, and S. C. McClain, "First results from a dual photoelastic-modulator-based polarimetric camera," Appl. Opt. **49**, 2929–2946 (2010).
15. R. A. Chipman, "Polarimetry," in *Handbook of Optics*, M. Bass, ed. (McGraw-Hill, 1995), Vol. **2**, chap. 22.
16. D. H. Goldstein, *Polarized Light* (CRC Press, 2011).
17. R. A. Chipman, "Structure of the Mueller calculus," Proc. SPIE **4133**, 1–9 (2000).
18. R. A. Chipman, W.-S. T. Lam, and G. Young, *Polarized Light and Optical Systems*, 1st ed. (CRC Press, 2018).
19. J. L. Pezzaniti and R. A. Chipman, "Mueller matrix scatter polarimetry of a diamond-turned mirror," Opt. Eng. **34**, 1593–1598 (1995).
20. B. J. DeBoo, J. M. Sasian, and R. A. Chipman, "Depolarization of diffusely reflecting man-made objects," Appl. Opt. **44**, 5434–5445 (2005).
21. R. M. A. Azzam, "Photopolarimetric measurement of the Mueller matrix by Fourier analysis of a single detected signal," Opt. Lett. **2**, 148–150 (1978).
22. R. A. Chipman, "Polarimetric impulse response and polarimetric transfer function for time-sequential polarimeters," Proc. SPIE **1317**, 223–241 (1990).
23. D. H. Goldstein, "Mueller matrix dual-rotating retarder polarimeter," Appl. Opt. **31**, 6676–6683 (1992).
24. R. M. A. Azzam and A. G. Lopez, "Accurate calibration of the four-detector photopolarimeter with imperfect polarizing optical elements," J. Opt. Soc. Am. A **6**, 1513–1521 (1989).
25. V. L. Gamiz, "Performance of a four-channel polarimeter with low-light-level detection," Proc. SPIE **3121**, 35–46 (1997).
26. T. A. Germer, "Polarized light diffusely scattered under smooth and rough interfaces," Proc. SPIE **5158**, 193–204 (2003).
27. D. Barrick, "Rough surface scattering based on the specular point theory," IEEE Trans. Antennas Propag. **16**, 449–454 (1968).
28. T. A. Germer, "SCATMECH: polarized light scattering C++ class library," 2021, https://pages.nist.gov/SCATMECH/docs/index.htm.
29. S. N. Savenkov, R. S. Muttiah, E. A. Oberemok, A. V. Priezzhev, I. S. Kolomiets, and A. S. Klimov, "Measurement and interpretation of Mueller matrices of barley leaves," Quantum Electron. **50**, 55 (2020).
30. K. M. Mitzner, "Change polarization on reflection from a tilted plane," Radio Sci. **1**, 27–30 (1966).
31. C. Bohren and D. Huffman, "Electromagnetic theory," in *Absorption and Scattering of Light by Small Particles* (Wiley, 1998), Sect. 2, pp. 12–56.
32. B. Smith, "Geometrical shadowing of a random rough surface," IEEE Trans. Antennas Propag. **15**, 668–671 (1967).
33. D. E. Aspnes and A. A. Studna, "Dielectric functions and optical parameters of Si, Ge, GaP, GaAs, GaSb, InP, InAs, and InSb from 1.5 to 6.0 eV," Phys. Rev. B **27**, 985–1009 (1983).
34. T. A. Germer, "Full four-dimensional and reciprocal Mueller matrix bidirectional reflectance distribution function of sintered polytetrafluoroethylene," Appl. Opt. **56**, 9333–9340 (2017).
35. W. A. Allen, H. W. Gausman, and A. J. Richardson, "Willstätter-Stoll theory of leaf reflectance evaluated by ray tracing," Appl. Opt. **12**, 2448–2453 (1973).
36. J. C. Lagarias, J. A. Reeds, M. H. Wright, and P. E. Wright, "Convergence properties of the Nelder–Mead simplex method in low dimensions," SIAM J. Optim. **9**, 112–147 (1998).
37. B. J. Frey, D. B. Leviton, T. J. Madison, Q. Gong, and M. Tecza, "Cryogenic temperature-dependent refractive index measurements of N-BK7, BaLKN3, SF15, and E-SF03," Proc. SPIE **6692**, 31–42 (2007).